GT2023-100405

HEAT TRANSFER AND FILM COOLING IN AN AGGRESSIVE TURBINE CENTER FRAME

Patrick R. Jagerhofer[1], Tobias Glasenapp[2], Bastian Patzer[2], Emil Göttlich[1]

[1]Graz University of Technology, Graz, Austria
[2]MTU Aero Engines AG, Munich, Germany

ABSTRACT

This paper investigates the heat transfer coefficient and the film cooling effectiveness in a turbine center frame (TCF). The TCF is a duct connecting the high-pressure turbine (HPT) to the low-pressure turbine (LPT) and is equipped with non-turning airfoils (struts). The TCF is operated in a product-representative 1.5-stage test turbine setup working under Mach-number-similarity. Upstream of the TCF, an unshrouded HPT is operated with four individually adjustable purge flow injections through the forward and aft cavities on the hub and tip of the rotor.

The heat transfer coefficient and the purge film cooling effectiveness are measured on the hub and the non-turning struts of the aerodynamically aggressive TCF using infrared thermography and tailor-made heating foils. To further extend the film cooling investigation, the seed gas concentration technique, in conjunction with the heat-mass transfer analogy, is used as a second film cooling measurement technique. Seeding the HPT cavities with different foreign gases reveals every individual purge flow's contribution to the global film cooling effectiveness in the TCF. Additionally, the seed gas technique extends the investigated area for film cooling to the optically inaccessible shroud of the TCF.

The heat transfer in the TCF was found to be dominated by secondary flow features of the upstream HPT. Longitudinal streaks of alternating high and low heat transfer were found on the hub connected to the number and position of the upstream HPT vanes. A similar pattern was found in the film cooling effectiveness, where the film cooling streaks were situated between the high heat transfer streaks. The film cooling coverage on the shroud was found to be even, symmetric and superior to the hub cooling performance, with around 10% less usage of purge mass flow.

1 INTRODUCTION

Given the stringent environmental targets in aviation [1, 2] and the most likely short-lived COVID-19-related reduction in aviation emissions [3], Joule process efficiencies and, thus, turbine inlet temperatures will need to increase even further. In most, if not all, future concepts of combustion-based aircraft turbines, the duct connecting the high-pressure turbine (HPT) to the low-pressure turbine (LPT) will be therefore subjected to increased thermal loads. This duct is referred to as the intermediate turbine duct or turbine center frame (TCF). The

TCF, exemplarily shown in Fig. 1 and 2, is an inherent component of modern high-bypass ungeared turbofan engines, such as the GP7000, GEnX or GE9X. The TCF is characterized by pronounced concave and convex bends facilitating the large radial offset between HPT and LPT in the shortest axial distance possible to avoid engine weight penalties. These aerodynamically "aggressive" designs, commonly employed by most engine manufacturers, result in quite an intricate pressure distribution through the TCF passage and corresponding velocity profiles that change dramatically through the duct. As shown in Fig. 1 and 2, the TCF typically features large non-lifting fairings in the shape of airfoils, which accommodate structural struts that support bearing loads and supply lines. *For the sake of simplicity, these large non-lifting airfoils or strut fairings are referred to as struts in this publication.* Given the increasing thermal loads, the complex inlet flow field from the upstream HPT, and the aggressive aerodynamic design prone to separation, there is lack of experimental data on heat transfer and film cooling in TCFs under engine-representative conditions.
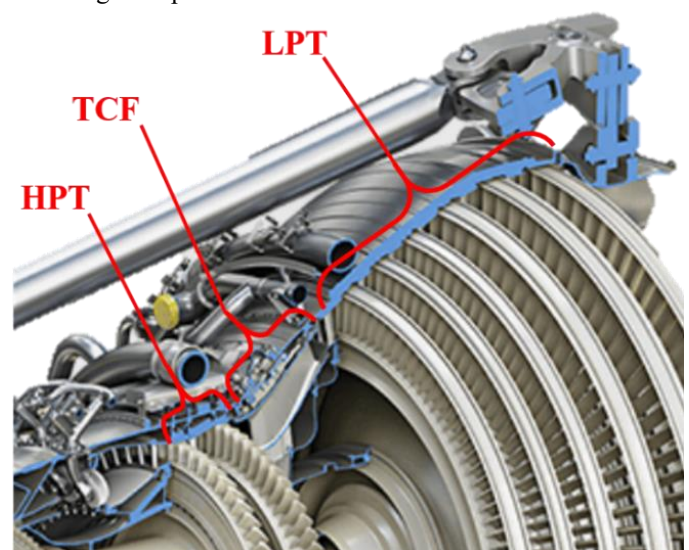

Figure 1: Turbine Center Frame (TCF) in a modern high-bypass ungeared turbofan engine (adapted from GE Aerospace [4])
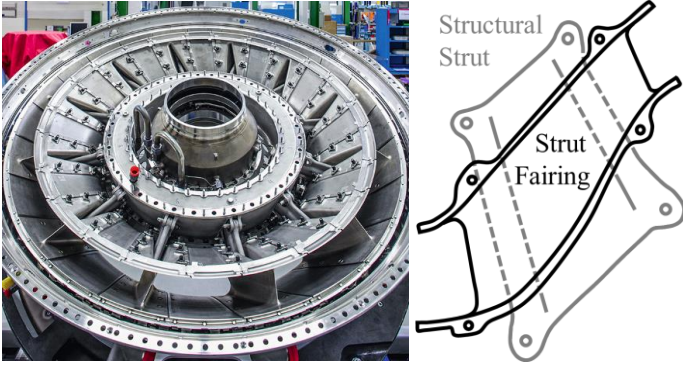
Figure 2: Left: TCF of the GEnx engine, adapted from [5]; right: sketch of a structural strut in a strut fairing

1.1 Literature Review

While most of the research on heat transfer and film cooling in turbomachinery focuses on simplified geometries, combustors, nozzle guide vanes and HPTs, only a few studies investigate the thermal behavior of TCFs. One of the first detailed heat transfer investigations in turbines were conducted by Graziani et al. [6] and Hylton et al. [7] in large-scale cascades. Already these early investigations from the 1980s showed that secondary flows highly influence the heat transfer in turbines and that inlet flow conditions must be carefully considered in the experiment. Studies on film cooling date back even further to the 1960s, when Hartnett et al. [8] proposed a correlation for flat plate slot film cooling, which later was used by Bogard and Thole [9] to correlate with more recent results. However, Bogard and Thole [9] also emphasized that conditions in real turbine applications lead to significant deviations from such flat plate experiments. Thole and Knost [10] and Suryanarayanan et al. [11] showed on stator and rotor endwalls that secondary flows highly influence the film cooling effectiveness. In turn, Zerobin et al. [12] reported for a turbine stage that the purge flows, which are injected through the HPT wheelspace cavities into the main flow, intensify and radially move the passage vortices, highlighting the mutual influence of purge flows and secondary flows. Ito et al. [13] showed for cooling films with lower momentum than the main flow, as is commonly the case for purge flows, that the cooling performance is superior on convex and inferior on concave surfaces. More recent investigations holistically combined heat transfer and film cooling investigations and moved on to more engine-representative test rigs with advanced and miniaturized measurement techniques. Hummel et al. [14] conducted combined heat transfer and film cooling investigations on a three-dimensionally contoured stator endwall. They showed that secondary flows caused localized heat transfer intensifications and non-uniformities in the cooling film. Additionally, they reported up to 100% heat transfer intensification due to cooling flow injection.

Scaling the film cooling effectiveness from the often low density ratios of experimental conditions, DR≈1, to the high density ratios of turbine operation, DR≈1.5-2, is an inherent problem of film cooling research. This is especially true for conventional film cooling applications with rows of small cooling holes and relatively high blowing ratios, M>0.5. For attached cooling films with low blowing ratios, M<0.2(0.5), as is mostly the case for HPT purge flows, the consensus exists that the influence of the density ratio is minimal [9, 15]. If foreign gases are used as coolants, the advective capacity ratio, ACR, was shown to be the superior scaling parameter [16].

1.2 Turbine Center Frames

The investigated engine component of this study, the TCF, has been extensively studied aerodynamically, as reviewed by Göttlich [17]. Recent studies dealt with the interaction of HPT purge flows with HPT secondary flows and their subsequent impact on the losses in the downstream TCF [12, 18]. Patinios et al. [19] used seed gas concentration measurements to track the migration of the HPT purge flows in a TCF similar to the one investigated in this study. They found that the stage vorticity of the HPT dictates the migration and dilution of the purge flows as they pass through the TCF. It was also found that the HPT aft hub and aft tip purge flows are forming high concentration boundary layers on the hub and the shroud surfaces at the TCF inlet and, therefore, bear a significant film cooling potential for the TCF. Please note that cooling and purge flows emanate from the same source (compressor bleed) and, therefore, bear a comparable cooling potential. This unplanned or serendipitous cooling effect (from a design point of view) is sometimes referred to as "phantom cooling", which is investigated in this study. Patinios et al. [19] also confirmed the observation of Zerobin et al. [18] that the aft hub purge flow is collected into discrete "purge streaks" by pairs of counter-rotating vortices from the upstream HPT.

As far as the authors are aware, there is only one full surface coverage investigation on heat transfer in a TCF that features realistic inflow conditions of an upstream HPT. Arroyo Osso et al. [20] measured the heat transfer coefficients on the surface of the hub, the non-turning struts and the shroud of the TCF under Reynolds-similarity in the low-speed, large-scale turbine facility at Chalmers University in Sweden. Their results showed longitudinal streaks of high and low heat transfer on the hub caused by pairs of counter-rotating vortices of the upstream HPT flow field. They also found a laminar to turbulent transition on the struts attenuated by secondary flow features closer to the endwalls. Since their turbine was unpurged, no film cooling investigations were made in the TCF.

To expand the understanding of the thermal behavior of TCFs, a series of experimental investigations were conducted at the Institute of Thermal Turbomachinery and Machine Dynamics (ITTM) at Graz University of Technology. First, a sector-cascade rig of a TCF with purge slots and clean inflow (no HPT upstream) was built to gain a fundamental understanding of the flow physics governing heat transfer and film cooling in TCFs [21]. At nominal purge rates, a significant cooling potential of up to η=0.4 was found for the HPT aft hub cavity. The heat transfer results were validated against aerodynamic measurements of Steiner et al. [22], and the heat transfer and film cooling distributions were found to be heavily influenced by secondary flow features in the duct. Next, a parameter study [23] was

conducted on the sector rig. There, the improvement of film cooling, but also the intensification of heat transfer with increasing purge blowing ratios, was investigated, as well as the influence of purge swirl. A correlation was established, capable of collapsing the centerline film cooling effectiveness along the hub for all investigated blowing ratios. This sector rig was also used to develop, improve and prepare the heat transfer and film cooling measurement technique [24] used in this study.

These aforementioned studies were conducted to pave the way for the heat transfer and film cooling measurements presented in this paper, featuring a fully purged, Mach-similar one-stage HPT operating upstream of the aerodynamically aggressive TCF. The measurements were conducted in the institute's Transonic Test Turbine Facility (TTTF) under engine-representative conditions. This study presents full surface coverage heat transfer and purge film cooling data in the TCF on the hub and the struts and point-wise film cooling data on the shroud, together with an in-depth explanation of the HPT flow fields' impact on the thermal behavior of the TCF.

1.3 HPT Stage Vorticity

As Zerobin et al. [12] explained in their work, the vorticity field of a turbine stage results from the superposition of the stator and rotor vorticity shown in Fig. 3. In a fixed frame of reference, the upper passage vortex (UPV_N clockwise=blue) and the lower passage vortex (LPV_N anticlockwise=red) of the stator can be found at fixed radial and circumferential positions shown in the bottom left vorticity field. The rotating vortical structures of the rotor, however, appear as circumferential bands in a time-averaged fixed frame of reference. When superimposing both vorticity fields, one obtains the stage vorticity as it is found at the TCF inlet, where the bands of constant rotor vorticity are periodically modulated by the stationary vortical structures of the stator. This modulation leads to a splitting of the negative (blue) vorticity band of the lower passage vortex of the rotor (LPV_R) into discrete vortices with the same periodicity as the vanes. This finally results in counter-rotating vortex pairs consisting of LPV_N and LPV_R close to the hub at the TCF inlet.

2 EXPERIMENTAL SETUP

2.1 Test Rig

All measurements were conducted in the Transonic Test Turbine Facility (TTTF) at Graz University of Technology. The TTTF is a cold-flow open-circuit Mach-similar turbine test facility, continuously operated by a 3 MW compressor station upstream and a 0.6 MW suction blower downstream. Additionally, a three-stage radial compressor that brakes the tested HPT recuperates its pressurized air by feeding it back into the pressurized main air supply of the facility.

The 1.5-stage setup tested in this study consists of an uncooled (no cooling holes or trailing edge cooling) but fully purged, unshrouded HPT stage that is aerodynamically representative of a second-stage HPT engine. This HPT is followed by the investigated aerodynamically aggressive TCF, where the so-called phantom cooling effect of the HPT purge flows will be investigated. After the TCF, an LPT vane row completes the 1.5-stage setup.
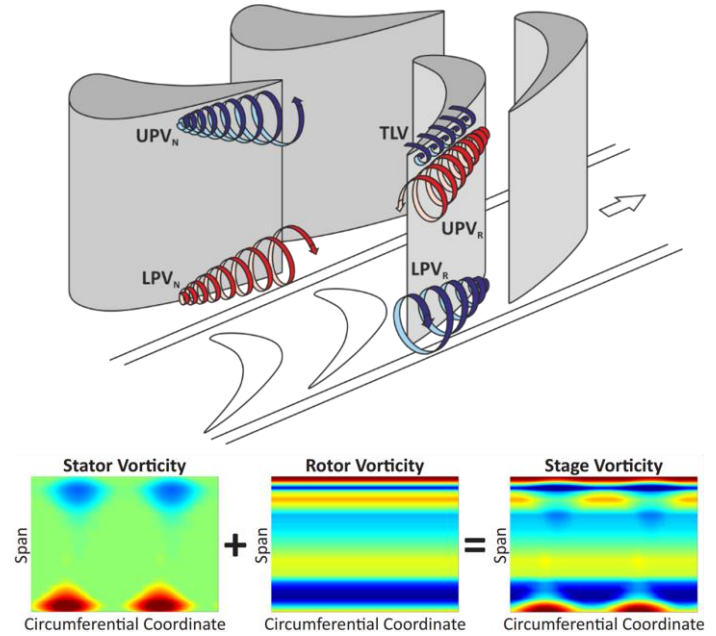

Figure 3: Sketch of the superposition of stator and rotor vorticity (adapted from Zerobin et al. [18])

The 1.5-stage setup, shown in Fig. 4, was tested under engine-representative operating conditions with matching HPT pressure ratio, Strouhal number and corrected speed. For more information about the facility and its operation, the interested reader is referred to Erhard et al. [25] and Neumayer et al. [26].

The four purged cavities of the HPT rotor span over the full annulus and are shown in the cross-section of the test vehicle in Fig. 4. The purge air is supplied by an auxiliary 1.1 MW compressor station and then fed through a temperature and mass flow conditioning station described in Steiner et al. [27]. The hub purge flows are fed into the forward (FWD) and aft (AFT) wheelspaces and then injected through product-representative rim seal geometries into the main flow. The FWD and AFT tip purge flows are injected through axial slots into the main flow.

2.2 Operating Conditions

The operating parameters of the turbine and the film cooling parameters of the purge flows are shown in Table 1. Three test cases with different purge settings at a constant turbine operating point were investigated. The uncertainties of the operating point parameters are given in the brackets next to the values. The no purge case is the uncooled baseline for the film cooling measurements. The CO_2 purge case was investigated to confirm the negligible influence of purge density ratio, DR, variations at the low blowing ratios, M, of purge flows. For this purpose, the AFT hub cavity was purged with a mixture of air and 36 mass-percent CO_2 while all other operating conditions were held constant.
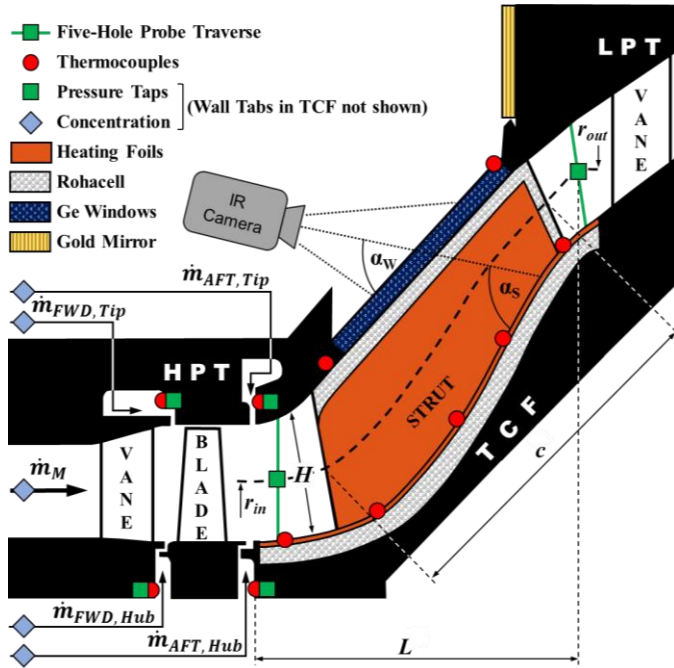
Figure 4: Test section with instrumentation (adapted from Patinios et al. [19])

2.3 Test Section Geometry and Instrumentation

Fig. 4 also shows the (due to confidentiality reasons distorted) TCF geometry. The ratio of radius change to axial duct length, $\Delta r/L$, indicates the aerodynamic aggressiveness of TCFs. With $\Delta r/L$ larger than 0.5, this TCF is representative for modern direct-drive two-spool turbofan engines. The outlet-to-inlet area ratio is bigger than one, indicating that the TCF is a diffuser. The thick non-turning struts have a chord-to-axial duct length ratio, c/L of 0.822. Since the HPT vane-to-TCF strut ratio is exactly four, the flow field in every TCF passage is the same.

The green squares with solid green lines in Fig. 4 denote five-hole probe (5HP) area traverses at the TCF inlet and outlet planes. The five-hole probes were manufactured and calibrated by the Institute of Jet Propulsion and Turbomachinery, RWTH Aachen University. At the TCF inlet plane, a so-called pseudo-traverse was performed. Due to geometrical restrictions, it was impossible to accommodate a circumferential traversing system for the 5HP. Instead, the 5HP was only radially traversed at the TCF centerline, and the HPT vanes were circumferentially traversed over 1.2 vane pitches. The drawback of this pseudo-traverse is that any upstream effects of the struts are missed. However, Faustmann and Göttlich [28] showed that such upstream effects are minor, and the results of pseudo and conventional traverses are comparable. A more thorough explanation of the 5HP measurement technique, data reduction and accuracy considerations can be found in Sterzinger et al. [29].

The green squares and red circles in Fig. 4 denote static pressure and temperature measurements, respectively. In the cavities, pressures and temperatures were monitored at at least three circumferential positions to ensure circ. uniformity.

Table 1: Operating conditions

Operating Parameter	Test Case		
	No Purge	Nominal Purge	CO$_2$ Purge
Mach number at TCF inlet, Ma		0.5	($\pm$1%)
Rotational speed HPT, n		9600 rpm	($\pm$0.1%)
Main mass flow, $\dot{m}_M$		13.2 kg/s	($\pm$2%)
Rig total pressure ratio, π_{Rig}		2.6	($\pm$0.5%)
Reynolds number, Re_c		>10^6	($\pm$1%)
FWD Hub — Blowing ratio, M	0	0.25	0.25
Density ratio, DR	-	1.46	1.46
Momentum flux ratio, I	0	0.043	0.043
Advective cap. r., ACR	0	=M	=M
AFT Hub — Blowing ratio, M	0	0.11	0.12
Density ratio, DR	-	1.05	**1.21**
Momentum flux ratio, I	0	0.012	0.012
Advective cap. r., ACR	0	=M	0.113
FWD Tip — Blowing ratio, M	0	0.59	0.59
Density ratio, DR	-	1.70	1.70
Momentum flux ratio, I	0	0.203	0.203
Advective cap. r., ACR	0	=M	=M
AFT Tip — Blowing ratio, M	0	0.23	0.23
Density ratio, DR	-	1.02	1.01
Momentum flux ratio, I	0	0.052	0.052
Advective cap. r., ACR	0	=M	=M

The AFT hub cavity temperature was more extensively measured with altogether nine thermocouples circ. spread over two radial positions to accurately quantify the reference purge temperature for the film cooling effectiveness.

Fig. 4 also illustrates how the heat transfer and film cooling measurement technique was incorporated into the TCF module. The measurement technique consists of a quasi-adiabatic surface covered with tailor-made heating foils observed with infrared (IR) thermography. The optical access was enabled by two trapezoidal broad-band antireflection-coated germanium windows (BBAR-GE) in the shroud of the TCF. The quasi-adiabatic surface was realized with an approx. 10mm thick Rohacell insert on the hub and a Rohacell strut with a thin structural metal core. Heat loss through the Rohacell parts was monitored at the thinnest positions with thermocouple pairs above and below the Rohacell material (not shown in Fig. 4) and was always less than 2.8%. The overall six heating foils were tailored to the strut, fillet and hub geometry and were designed to deliver constant heat flux. The surfaces covered with heating foils are marked orange in Fig. 4. Compared to the previous studies in a sector rig of Jagerhofer et al. [21, 23], the foils were further improved in terms of surface coverage and heat flux homogeneity. The heating foils were supplied with electricity from contacting lugs far outside the field of view. The strut heating foil fully wraps around and covers both sides of the strut to prevent any heat loss to the other (not observed) side. An in-

depth explanation of the layers and the working principle of the heating foils is presented in Jagerhofer et al. [24].

The hub and strut surfaces were observed with a FLIR T650-sc IR camera with an uncooled microbolometer sensor with 20 mK sensitivity. To further increase the measurement accuracy, the hub and strut surfaces were equipped with 15 tailor-made single-calibrated surface thermocouples. These in-situ thermocouples were thin enough to sit on the heating foils without disturbing the flow. The in-situ thermocouples at the hub centerline are shown as red circles in Fig. 4. Necessary for calibration, the shroud and the window temperatures were also measured with single calibrated thermocouples at multiple axial locations. The heating foils together with the in-situ surface thermocouples were spray-painted with the high emissivity paint Nextel Velvet 811-21.

To maximize the observable area of the IR camera, a gold-coated mirror was mounted on the casing of the rig, as illustrated in Fig. 4. With this mirror, it was possible to observe the hub surface until the hub cavity exit, which is the most crucial area for the hub film cooling investigations. Any additional error due to the imperfect reflectivity of the mirror was compensated by an in-situ thermocouple placed on the heating foils in the field of view of the mirror. To cover the hub and strut surfaces, 21 different camera angles were needed. This was realized with a tailor-made 5-axis traversing system, capable of moving the camera in the very confined environment of the rig. The relatively hot turbine casing upstream of the TCF was insulated, and every possible source of background radiation was shielded using stretchable cloths that moved together with the traversing system.

To further improve the accuracy of the film cooling measurements on the hub and also to obtain film cooling data on the optically inaccessible shroud, the seed gas concentration technique was introduced as a second measurement technique. By seeding the FWD and AFT cavities with different tracer gases (CO_2 and N_2O) and analyzing samples drawn from the overall 60 hub, 54 strut and 43 shroud pressure wall taps in an adjacent TCF passage, the film cooling effectiveness was measured point-wise with very high accuracy. The samples for the main flow and the purge flow concentrations were taken far upstream and are indicated as blue diamonds in Fig. 4. The positions of the pressure wall taps will be shown later in the results section. The gas samples were analyzed using a two-channel Siemens Ultramat 6E gas analyzer. For a more thorough introduction to this measurement technique, the reader is referred to Patinios et al. [19]. The combination of the IR camera and the tracer gases was carefully chosen to avoid any overlapping of the camera's spectral range with the spectral emissivity bands of the gases.

2.4 Data Reduction

The data reduction of the raw IR images together with the supplied power to the heating foils into the surface maps of heat transfer coefficient, h, and film cooling effectiveness, η_{IR}, is thoroughly described in the open access publication Jagerhofer et al. [24] and will therefore only be discussed briefly here.

The 21 IR images acquired for one temperature field covering the hub and the struts undergo the sequence of 2D-3D mapping, pre-calibration, overlapping and in-situ calibration. An essential step of the pre-calibration is the correction for the variability of paint surface emissivity, ε_S, with surface viewing-angle, α_S, and the variability of window transmissivity, τ_S, with window viewing-angle, α_W, shown in Fig. 5. These curves were acquired in a vacuum chamber with the calibration targets being painted with the same high emissivity paint as the TCF hub and strut surfaces. Also, the same germanium IR windows were used and heated to the same temperature as during operation in the rig. After the 2D-3D mapping, the pre-calibrated IR images are overlapped to a temperature field spanning the hub and struts and finally in-situ calibrated using the 15 tailor-made surface thermocouples on the heating foils.

The supplied heat flux of the heating foils, $\dot{q}$, is essentially the supplied electrical power divided by the area of the foils. The heat flux corrections can again be found in Jagerhofer et al. [24]. In contrast, only the copper resistance correction has been used here, and the conduction correction through the strut and heat flux inhomogeneity correction are no longer necessary due to the improved design of the heating foils.

Finally, h is then calculated by dividing the supplied heat flux of the heating foils, $\dot{q}$, with the temperature difference between the heated surface temperature, T_S, and the unheated quasi-adiabatic surface temperature $T_{S,ad}$.

$$h = \frac{\dot{q}}{T_S - T_{S,ad}} \qquad (1)$$

The adiabatic film cooling effectiveness originating from the IR measurements, η_{IR}, is defined as

$$\eta_{IR} = \frac{T_{S,ad} - T_{S,ad}'}{T_P - T_{S,ad}'} \qquad (2)$$

where the prime $'$ denotes quantities of the no purge test case and T_P is the AFT hub purge temperature.

The definition of T_P bears some ambiguity because all purge flows were turned off in the no purge case in order to keep the rotor tip gap constant. If only the AFT hub purge had been turned off, the then uncooled rotor disc would have expanded in the
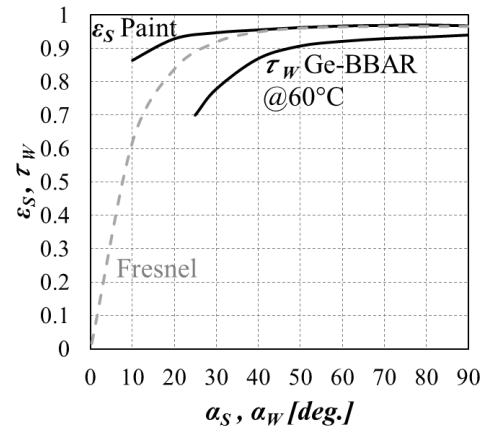

Figure 5: Paint emissivity and window transmissivity as a function of observation angle

cooled casing, leading to a dangerously tight tip clearance and a significant operating point deviation. As shown later in the results, the influence of the other three purge flows on the hub film cooling is negligible. However, for the sake of completeness, the albeit low FWD cavities' cooling performance will be considered in the seed gas technique described in the following.

To remove the ambiguity around T_P for η_{IR} on the hub, the seed gas concentration technique was used as in-situ calibration ground truth for the thermographic η_{IR} results. Additionally, this technique allows η measurements on the optically inaccessible shroud. Two seeding gases, CO_2 and N_2O, were used to seed the FWD and AFT purge flows simultaneously. First, the hub cavities and then the tip cavities were seeded. This halved the measurement time and made it possible to split the film cooling results into the contribution of all four purge flows. Please note that there is no cross-talk in the IR spectrum of the two seeding gases, enabling the simultaneous acquisition with the two-channel gas analyzer. Furthermore, the mass transfer analogy is not relying on the definition of driving temperatures, which would have been especially challenging for the FWD cavities, where the purge flows cool down due to their expansion over the rotor. Another challenge for the definition of driving temperatures is the dissipational heat up of the hub purge flows in the rotating wheelspace cavities. Seed gas is not sensitive to any of those error sources. Since the seeding concentration of the purge flows was below 8% and the flow after the HPT is highly turbulent, the turbulent Lewis number ratio is close to unity in this setup. This allows the application of the heat-mass transfer analogy [30] and that the film cooling effectiveness from seed gas, η_{SG}, can be used as the ground truth for an in-situ calibration of η_{IR}. The definition of η_{SG} is analogous to the definition of η_{IR} with concentrations instead of temperatures:

$$\eta_{SG,FWD/AFT} = \frac{conc._S - conc._M}{conc._P - conc._M} \qquad (3)$$

Here, $conc._S$ is the concentration sampled from the TCF wall pressure taps, $conc._M$ the mainstream and $conc._P$ the purge concentration of one of the four seeded purge flows.

The in-situ calibration of η_{IR} with η_{SG} on the hub and struts is analog to how IR temperatures were calibrated with in-situ thermocouples, explained in Jagerhofer et al. [24]. First step: the FWD and AFT effectivenesses $\eta_{SG,FWD}$ and $\eta_{SG,AFT}$ are combined into the total effectiveness η_{SG} using the formula of Sellers [31]:

$$\eta_{SG} = 1 - (1 - \eta_{SG,FWD})(1 - \eta_{SG,AFT}) \qquad (4)$$

The result of Eq. 4 exists only at the wall tap locations and is the in-situ ground truth for the hub and struts and the final η result on the optically inaccessible shroud. Second step: the in-situ calibration offset is calculated as the difference between η_{IR} and η_{SG} at the position of the wall taps. Third step: this point-wise in-situ calibration offset is spatially interpolated to obtain a continuous field covering the hub and strut surfaces. Final step: this offset field is subtracted from the η_{IR} field. This results in the final η field, which contains the exact value of η_{SG} at the taps but also the variations of η_{IR} between the taps. In other words, the η

in-situ calibration combines the advantage of high accuracy and robustness against ambiguous temperature definitions of the (point-wise) seed gas technique and the high spatial resolution of the IR technique.

2.5 Measurement Uncertainty

The uncertainties shown in Fig. 6 and 7 were calculated according to the *guide to the expression of uncertainty in measurement* [32] and are given as 95% confidence intervals (twice the standard deviation). An extensive analysis of the presented uncertainties of h and η_{IR} can be found in Jagerhofer et al. [24] and of η_{SG} in Patinios et al. [19]. For this study, the uncertainties were analogously obtained.

Fig. 6 shows the uncertainty of h averaged over the circumference along the hub and at the strut midspan. Please note that the average uncertainty of both strut sides is shown here. The variation of the uncertainty, U_h, is essentially a function of the temperature difference, $T_S-T_{S,ad}$. U_h is higher in regions where the heat transfer, h, is high, and thus the obtained temperature difference at constant heat flux is low.

Fig 7 compares the uncertainty of both measurement techniques for the film cooling effectiveness. The seed gas concentration technique is nearly an order of magnitude more accurate than the infrared method, but its data is only available at the pressure taps. This underlines the importance of the above-mentioned in-situ calibration, where η_{IR} is combined with η_{SG} to form the final η field. The uncertainty of (the in-situ calibrated) η lies between the seed gas and infrared uncertainty. At the position of a wall tab, the uncertainty of η equals the uncertainty of η_{SG}. The uncertainty of η_{IR} could be seen as a very pessimistic upper boundary estimation for the uncertainty of η on the surface between the wall taps.
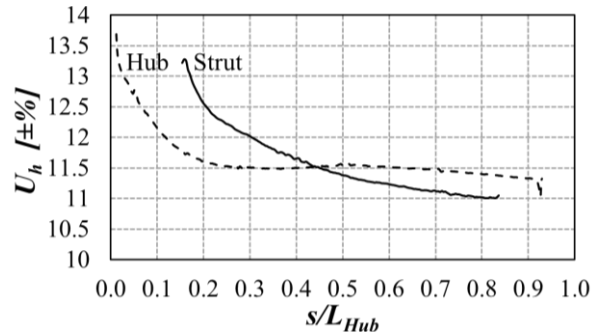

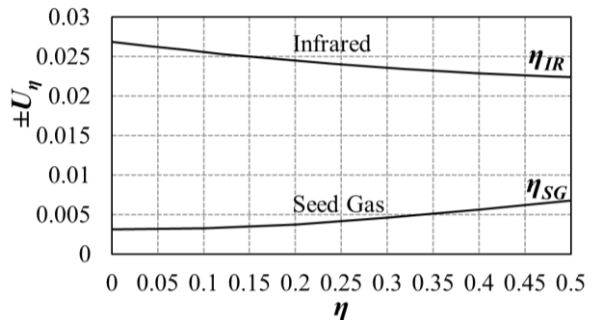**Figure 6: Uncertainty of *h* on the hub and the struts**

Figure 7: Uncertainty of *η* as a function of its value

Note that these measurement uncertainties are valid for the absolute measured values. The uncertainty in the differences between the investigated cases, which were measured in the same facility and with the same equipment, is smaller.

3 INLET FLOW CHARACTERIZATION

The contour plots in Fig. 8 of total pressure, P_0, (left) and streamwise vorticity, ω_{sw}, (right) were acquired using the aforementioned pseudo-traverse of a 5HP at the TCF inlet plane. The shown data originates from the nominal purge case, and the viewing direction is aft looking forward (ALF). Regions very close to the endwalls, where due to the 5HP head size measurements were not possible, are left in white. For confidentiality reasons, no absolute total pressure values can be given, and only total pressure differences are shown. The streamwise vorticity was calculated according to the well-established definition of Gregory-Smith [33]:

$$\omega_{sw} = \frac{V_x \cdot \omega_x + V_t \cdot \omega_t + V_r \cdot \omega_r}{\sqrt{V_x{}^2 + V_t{}^2 + V_r{}^2}} \quad (5)$$

In the fixed frame of reference of the time-averaged 5HP measurements, circumferential structures (bands) are induced by the HPT rotor and modulated by circumferentially fixed structures of the HPT stator. Zone 1 in the P_0 plot is a major loss region in the flow field at the TCF Inlet and, due to its vertical shape, connected to the stator vanes. As explained in Patinios et al. [19], the upper part of zone 1 is a result of the stator wake and the lower part is a result of secondary flow vortices of the vanes that are circumferentially stretched within the blade passage. The adjacent vertical zone 2 of high total pressure, in turn, represents the undisturbed core flow of the stator vanes. Zone 3 is a circumferential loss band caused by the viscous interaction of the rotor upper passage vortex (UPV-R) and the rotor tip leakage vortex (TLV). Zone 4 is the under-turned high-energy tip leakage flow, also observable as a band of very high streamwise vorticity.

In the lower third of the streamwise vorticity plot, the rotor lower passage vortex (LPV-R) and the stator lower passage vortex (LPV-N) can be seen. As described in the introduction
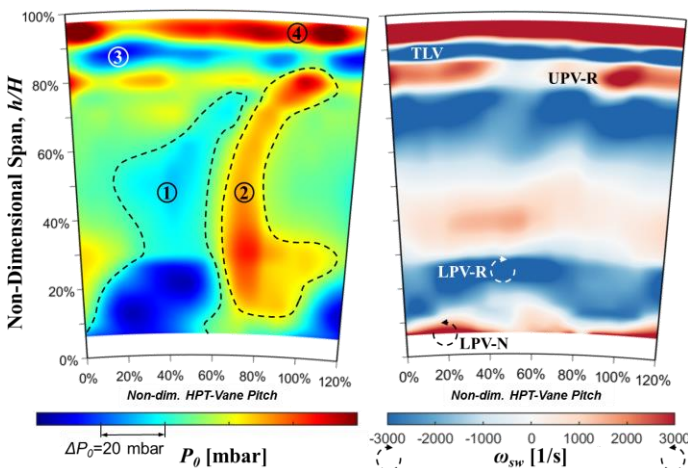
with Fig. 3, the circumferential band of the LPV-R splits up into discrete vortices due to its periodic modulation by the upstream stator vorticity field. Due to this mechanism, one counter-rotating vortex pair (LPV-R and LPV-N) exists for every stator pitch at the TCF inlet.

4 HEAT TRANSFER MEASUREMENTS

This section presents the measurement results of the heat transfer coefficient, h, and the film cooling effectiveness, η, together with 5HP measurements at the inlet and outlet plane. The values of h are always nondimensionalized with the maximum of the *no purge* case $h_{max}{}'$ for confidentiality reasons.

4.1 Heat Transfer Coefficient

Fig. 9 shows the heat transfer coefficient, h, distribution on the hub and the struts of the TCF for the nominal purge case overlaid with the total pressure measurement from Fig. 8 at the inlet plane. Additionally, absolute velocity isolines, V, are plotted as white solid lines at the inlet plane. The inlet plane field of Fig. 8 was repeated in the circumferential direction to fill the entire TCF inlet width. Please note that the inlet plane measurement results do not include any (albeit weak) upstream blockage effects due to the use of a pseudo-traverse. Therefore, the inlet plane 5HP results from Fig. 9 should only be seen as an aid to the discussion of the flow physics governing the heat transfer. The view is against the flow, looking through the TCF outlet into the TCF passage (tilted ALF). The measurement region covers the whole hub surface and the struts up to 80% channel height. Regions where no measurements were possible are left in white. This includes the borders between the heating foils in the fillet and two spots on the hub at the TCF exit due to a small coating ablation on the windows.

The heat transfer on the hub in the TCF is dominated by the outlet flow features of the HPT. On the hub at the TCF inlet, h shows a monotonical decrease in the axial direction typical for the formation of a new boundary layer at the hub cavity exit. Four distinct longitudinal streaks of high h marked with the dashed lines 1-4 in Fig. 9 coincide with the high P_0 zone linked to the undisturbed HPT vane core flow.

Figure 8: Total pressure (left) and streamwise vorticity (right) of nom. purge at the TCF inlet (the view is ALF.)
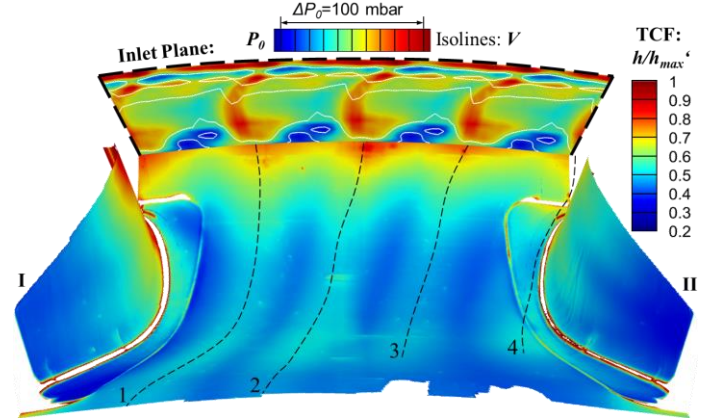

Figure 9: Heat transfer coefficient in the TCF of nominal purge, overlaid with the total pressure and velocity at the TCF inlet plane (the view is tilted ALF.)

7

The isolines of absolute velocity, V, at the TCF inlet plane also coincide with the high h streaks, where high velocity above the hub causes high h and vice versa. This explains the circumferential variation of h on the hub close to the TCF inlet, but it cannot fully explain why the high h streaks 1 and 2 exist through the whole length of the duct.

The circumferential difference in h from the peak to the adjacent valley of a streak equals ≈11 % of the local circumferential mean of h. This difference remains approximately constant throughout the hub length. If the streaks had been caused solely by the surplus of velocity and total pressure of the HPT vane core flow, the intensity of the streaks downstream of the TCF inlet should have weakened due to viscous mixing. This was shown by Jagerhofer et al. [24] in preliminary investigations of this TCF in a sector rig, where inlet pegs were installed at the TCF inlet: The imprint of the pegs' wakes on the h field on the hub was only observable until half of the hub length. Therefore, another mechanism must be driving these circumferential h variations on the hub.

Fig. 10 left shows the same view of the h distribution as Fig. 9, but now with the streamwise vorticity, ω_{sw}, at the inlet plane. Fig. 10 right shows an isometric view of the h distribution in the TCF and ω_{sw} at the outlet plane of the TCF. The inlet plane ω_{sw} stems again from the pseudo-traverse in Fig. 8, while the outlet plane ω_{sw} was measured with a true 5HP area traverse.

As mentioned above, one counter-rotating vortex pair (LPV-R and LPV-N) exists for every HPT stator pitch at the TCF inlet. The first pair from the left is labeled 4-b and 1-a in Fig. 10. These vortex pairs are still present in the TCF outlet plane close to the hub. It is now an anti-pair that causes a high h streak "to survive" and still be evident at the TCF outlet: e.g., anti-pair 1-a with 1-b is responsible for the high h streak 1. As Arroyo Osso et al. [20] explained, the anti-pairs push high momentum fluid toward the surface, squeeze the boundary layer and increase the wall shear stress and, consequently, the heat transfer. The opposite occurs circumferentially between the high h streaks, where the vortex pairs, e.g., 1-b and 2-a, lift off fluid from the surface, thicken the boundary layer, and decrease the wall shear stress and, consequently, the heat transfer. As very similar high h streaks were found by Arroyo Osso et al. [20] in a significantly less aggressive TCF (smaller $\Delta r/L$), these findings seem to be valid more generally for varying TCF geometries.

The individual behavior of the high h streaks can also be explained with the outlet ω_{sw} field. The third lower passage vortex of the HPT vanes, 3-b, is diminishingly weak at the TCF outlet. Therefore, Vortex 3-a has a weak partner and the corresponding high h streak 3 diminishes earlier in the passage. The high h streak 4 impinges on the strut leading edge, then diverts to the left (ALF) into the passage and diminishes earliest. The vortices corresponding to streak 4, namely 4-a and 4-b, interact with the strut flow field and are situated very far apart at the TCF outlet, explaining the early diminishing of streak 4 in the passage. Vortex 4-b seems to have merged with the strut wake vorticity field. Overall, the longevity of the streaks throughout the passage can be explained by the vortex pairs (or anti-pairs) of the HPT vorticity field.
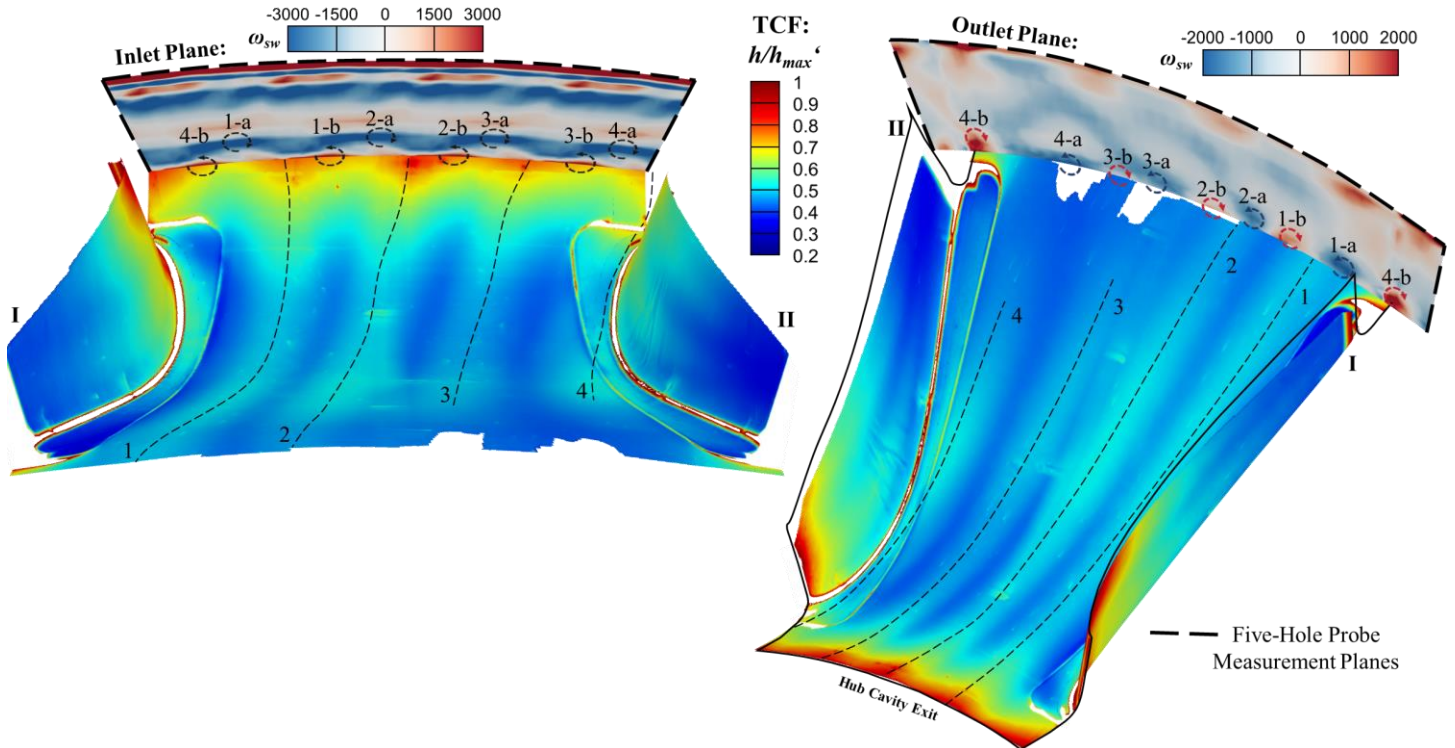

Figure 10: Heat transfer coefficient distribution in the TCF of nominal purge overlaid with the streamwise vorticity field at the TCF inlet plane (left) and outlet plane (right)

All four streaks migrate circumferentially to the left (ALF) as they pass through the TCF due to the yaw angle distribution at the HPT outlet. Close to the hub, the yaw angle is overturned, which is with the clockwise rotation of the HPT to the left in the ALF orientation.

The circumferentially averaged heat transfer coefficient along the unwound running length of the hub, s/L_{Hub}, is shown in Fig. 11. The averaging region is illustrated in the insert top right in the diagram, and all quantities are again nondimensionalized. All three investigated cases in Fig. 11 are presented and compared against the laminar and turbulent flat plate correlations for constant heat flux given by Çengel and Ghajar [34], calculated with the TCF inlet velocity and shown in Eq. 6 and 7:

$$Nu_s = h_s s/k = 0.453 Re_s^{0.5} Pr^{1/3} \qquad (6)$$

$$Nu_s = h_s s/k = 0.0308 Re_s^{0.8} Pr^{1/3} \qquad (7)$$

The overall behavior of h in all investigated cases is similar: a pronounced asymptotical decrease from the maximum at the hub cavity exit at $s/L_{Hub}=0$ until a local minimum of $h/h_{max}'=0.46$ is reached at $s/L_{Hub}=0.3$, followed by a weak increase to a local maximum of $h/h_{max}'=0.5$ at $s/L_{Hub}=0.5$ and finally a decrease until the TCF exit.

The nominal purge injection leads to a heat transfer intensification of approx. +10% compared to the no purge case close to the cavity exit, which fades out until $s/L_{Hub}=0.2$. After this position, the no purge case shows even slightly higher heat transfer than the nominal purge case. However, this weak effect could be attributed to the sensitivity of the averaging window's position, since it was found that the circumferential positioning of the high h streaks depends on the purge blowing ratios. This effect, also known as "purge-clocking", is described in detail by Zerobin et al. [18]. With increasing purge blowing ratios, the yaw angles at the TCF inlet also slightly increase, which in turn affects the migration of the high h streaks throughout the duct.
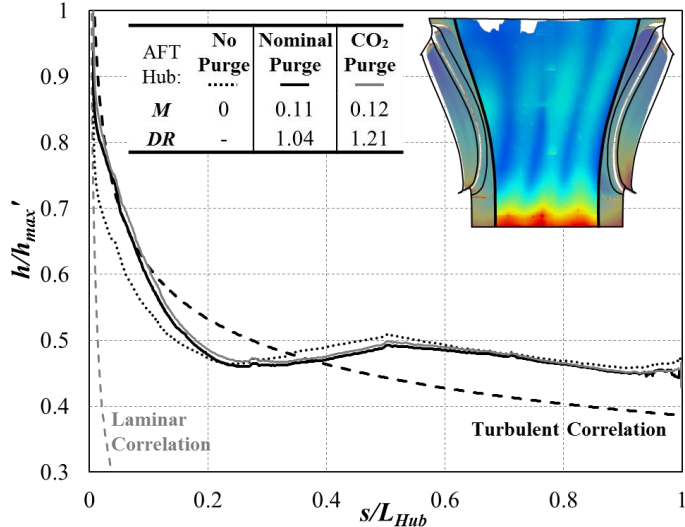
Figure 11: Circumferential average of the heat transfer coefficient along the hub surface for all test cases

Up to $s/L_{Hub}=0.1$, the nominal purge case shows excellent agreement with the turbulent boundary correlation, pointing toward the hypothesis that the injection of the aft hub purge flow leads to an immediate transition to turbulent flow at the hub cavity exit. The first data points of the no purge case at $s/L_{Hub}=0$ coincide with the laminar correlation. Then all cases deviate to lower values of h as the flow decelerates due to the positive pressure gradient towards the apex of the convex bend of the hub. After $s/L_{Hub}=0.3$, the heat transfer increases to higher values than the turbulent flat plate correlation as the flow accelerates after the apex of the convex bend and also due to the influence of the high h streaks.

The nominal purge and the CO_2 purge cases are practically collapsing, confirming the hypothesis of the negligible influence of different density ratios at low blowing ratios on h. The agreement between the nominal and the CO_2 purge case could, therefore, also be seen as an indicator of the repeatability of the experiments. Please note that, although not shown here, the nominal purge measurement was repeated on a different day during the campaign. The repetition variance was virtually equal to the variation between the herein-shown nominal and CO_2 cases.

The distribution of h on the struts is presented for the nominal purge case in Fig. 12. As mentioned above, the HPT vane to strut count is exactly four, making the flow in every TCF passage identical. Therefore, the measured sides of struts I and II, shown in Fig. 9 and 10, can also be seen as the two sides of the same strut, in the following referred to as "*the strut*". Fig. 12 (a) shows *the strut* in the forward looking aft (FLA) orientation, where the optically inaccessible leading edge is left white. Fig 12 (b) shows side I and (d) side II of *the strut*, where optically inaccessible regions or regions not covered with heating foils are again left white. Fig 12 (c) shows the pseudo-traversed 5HP measurements of total pressure, P_0, and velocity, V, aligned to the views (a), (b) and (d) of *the strut*. Due to the pseudo-traverse, the albeit weak upstream blockage effect of *the strut* is not included in the 5HP results, so they should only be seen as an aid for the following discussion.

As can be seen from the alignment of the 5HP measurements of the flow field with *the strut*, the high momentum and undisturbed core flow of the HPT vanes (Zone 2 in Fig. 8) impinges directly onto the strut leading edge. The highest h of the entire measurement region is found on side I of *the strut*, marked with a white +. This high h region results from the impingement of the very high P_0 and V zone, which is also marked with a white +. This very high P_0 and V zone is situated on a horizontal band of also relatively high P_0 and V, causing a high h streak on both strut sides, marked I-1 and II-1. The shape of the high momentum HPT vane core flow is marked with a dash-dotted line in Fig. 12 (c). The imprint of the left s-shaped dash-dotted line in (c) can be seen on the h distribution on strut side I, also marked with a dash-dotted line. The right bow-shaped line in (c) can also be seen on the h distribution on strut side II. The radially lower maximum of the s-shaped line in Fig. 12 (c) causes the second high h streak I-2 on strut side I.
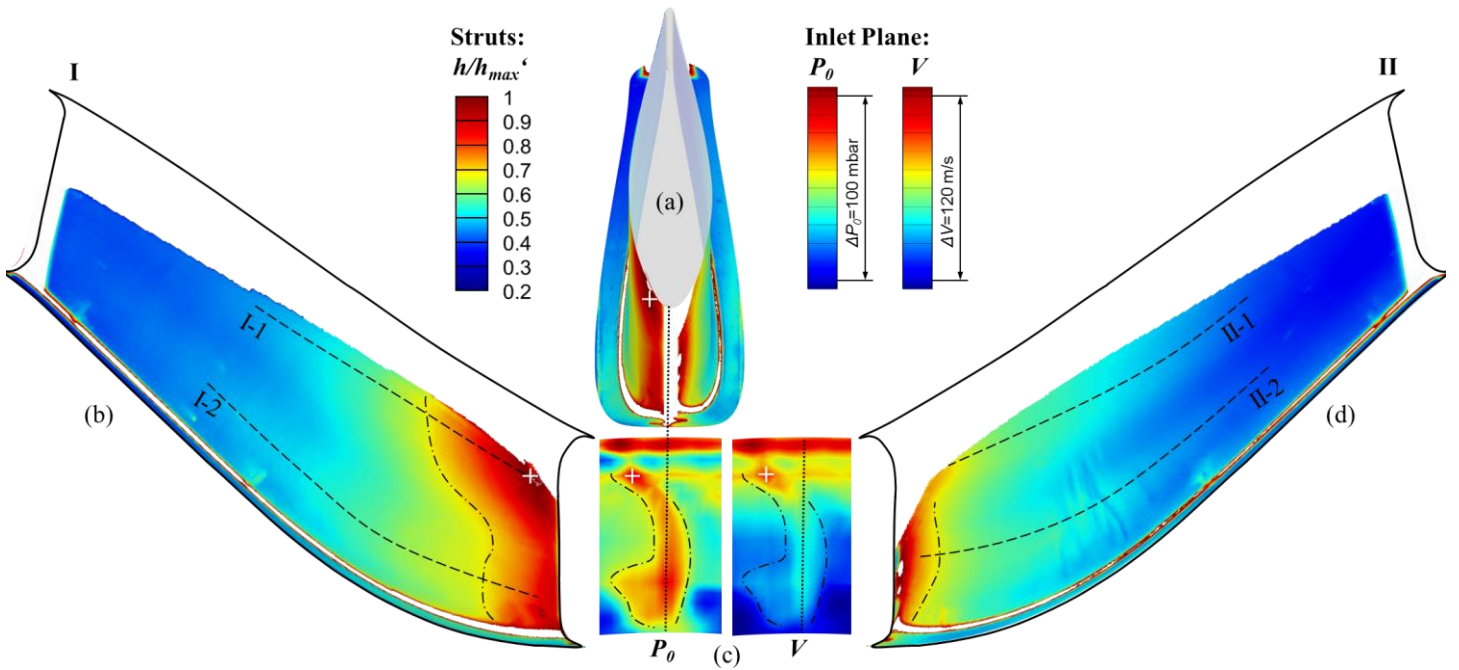
Figure 12: Heat transfer coefficient distribution on the strut: (a) front view (FLA), (b) strut side I, (c) total pressure and velocity field at TCF inlet (FLA), (d) strut Side II
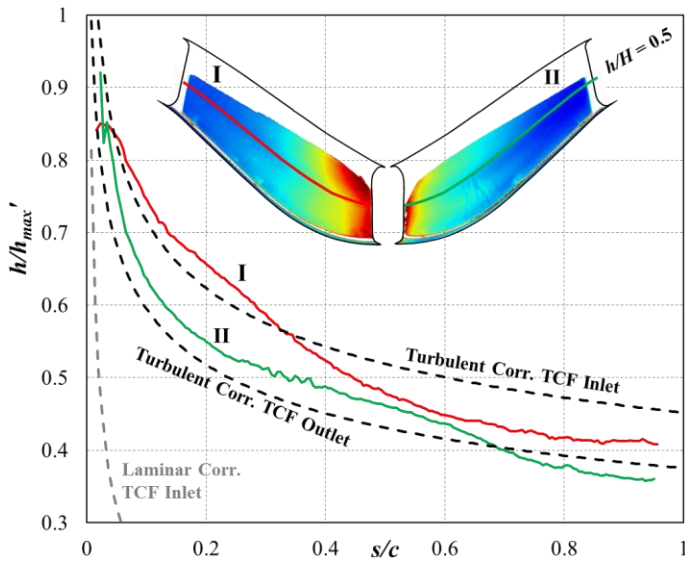

Figure 13: Chordwise variation of heat transfer coefficient along the midspan on strut sides I and II

Also, the imprint of the maximum of the bow-shaped line in Fig. 12 (c) causes the second high h streak II-2 on the other side of the strut (II). It can be concluded that the oncoming HPT flow dominates the heat transfer on *the strut* to such an extent that the h distribution can be seen as an imprint of the HPT flow field. Therefore, the circumferential positioning or clocking of the upstream HPT vanes is crucial for the heat transfer on *the strut*.

Fig. 13 shows the chordwise variation of h on both strut sides at midspan. The flat plate correlations from Eq. 4 and 5 are again shown as dashed lines, but here with an additional turbulent flat plate correlation calculated with the TCF outlet velocity.

No laminar-turbulent transition can be seen in the observable area, as no data coincides with the laminar correlation. The boundary layer seems to start turbulent on both sides of the strut due to their positioning in the high momentum core flow of the HPT vanes. The h distribution at the midspan of strut side I shows good agreement with the turbulent flat plate correlation calculated with the inlet velocity until s/c=0.3. Then it transitions to lower values and better agreement with the turbulent flat plate correlation calculated with the outlet velocity. The heat transfer at midspan on strut side II shows only on the very first data points some agreement with the inlet turbulent flat plate correlation before it then follows the turbulent correlation calculated with the outlet velocity. The average of the lines of side I and II in Fig. 13 would, therefore, agree best with the inlet flat plate correlation and then transition to the outlet flat plate correlation. This behavior was expected since the TCF is designed as a diffuser to decelerate the flow and recuperate static pressure.

4.2 Film Cooling Effectiveness

Following the detailed discussion of the heat transfer coefficients in the TCF, this section now addresses the (purge) film cooling effectiveness measurements. Fig. 14 shows the same view and the same ω_{sw} distribution at the inlet plane as Fig. 10 on the left, but now with the film cooling effectiveness, η, distribution of the nominal purge case on the hub and both strut sides. As described above, the herein shown η contours are the IR measurements in-situ calibrated with the seed-gas concentration technique. The traces of the high h streaks are again shown as dashed lines. As will be shown later, the film
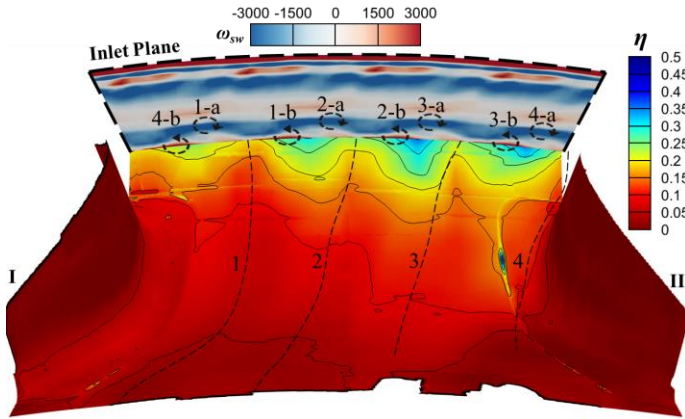
10

Figure 14: Film cooling effectiveness distribution in the TCF overlaid with the streamwise vorticity field at the TCF inlet plane (the view is tilted ALF.)

cooling contribution of the FWD hub purge is always less than 0.02, and the cooling effect on the hub will therefore be regarded as AFT hub purge cooling.

Interestingly, the cooling film coverage of the AFT hub purge flow also forms four distinct streaks. However, the streaks of high η are positioned circumferentially exactly between the high h streaks. This is an unfavorable combination, since the cooling is weakest where the heat transfer is strongest. The maximum film cooling effectiveness is as expected at the hub cavity exit (here hidden behind the inlet plane) and equals 0.5. From there, η drops quickly axially so that at the position of the strut leading edges, η is already below 0.2. After the strut leading edges, the film cooling distribution becomes asymmetric on the hub with higher values on the ALF right side. The film cooling effectiveness is negligibly low, $\eta \leq 0.05$, on both strut sides and most of the fillets.

Fig. 15 depicts the view onto the hub and the shroud surfaces with η distributions on top and static pressure, P_S, distributions at the bottom. The η distribution on the hub is the same as in Fig. 14. The η distribution on the shroud originates solely from the seed gas concentration measurements, η_{SG}, taken at the wall pressure taps, shown as black dots. No IR measurements were possible at the shroud due to its optical inaccessibility. Since the film cooling effectiveness from the seed gas concentration technique, η_{SG}, is only point-wise information, the natural neighbor interpolation [35] was used to create a surface distribution. Areas with too long distances between adjacent wall taps for a trustworthy interpolation are shaded white. The same procedure was done for the distribution of static wall pressure, P_S, at the bottom in Fig. 15 (measured from the same wall taps).

The circumferential static pressure variation at the hub cavity exit causes the AFT hub purge flow to exit the cavity already preferentially in four streaks. This is the first driver to cause the periodic non-uniformity of the cooling film. Then the above-mentioned vortex pairs of the HPT flow field collect the purge flow into even more distinct streaks, which is the second driver of the streak-shaped cooling film.
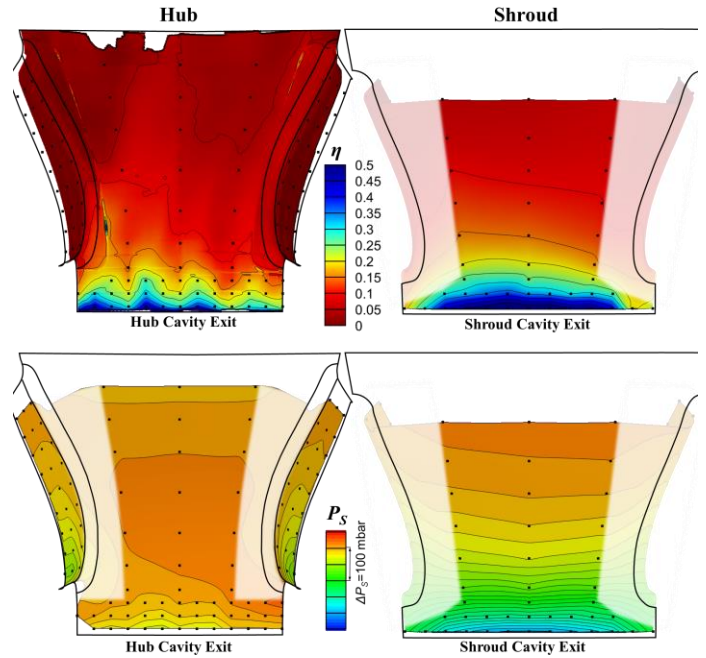

Figure 15: Top view of hub and shroud surfaces with distributions of film cooling effectiveness and static wall pressure, wall taps indicated as dots

For instance, while the above-mentioned anti-pair 1-a and 1-b in Fig. 14 sustain the high h streak 1, the pair 1-b and 2-a collect the purge air on the hub surface between the high h streaks 1 and 2. This explains why the high η streaks are situated between the high h streaks. Additionally, Patinios et al. [19] found out that the purge air is not only collected by the vortex pairs but also lifted off from the hub surface into lobes of high purge air concentration. Already at the TCF outlet, the center of these purge air lobes had detached from the hub surface. This underlines the detrimental influence of the HPT vortex pairs on the thermal load of the hub.

The asymmetry of the cooling film on the hub after the strut leading edges can be explained by the HPT's outlet yaw angle distribution. As mentioned above, the HPT has an over-turning outlet yaw angle close to the hub. Over-turning means to the right in the orientation of Fig. 15. This leads to a positive incidence on the right strut and hence to the asymmetric static pressure distribution on the hub between the struts, as can be seen in Fig. 15. This pressure distribution, in turn, forces the low momentum purge flow to migrate towards lower pressure, hence to the left in Fig. 15.

Further downstream after half of the strut length, a downward movement of the flow from the left strut to the hub exists, as found by Steiner et al. [22]. This downward flow movement sweeps away the cooling film on the hub next to the left strut and close to the TCF exit.

The static pressure and η distribution on the shroud are broadly symmetric. The film cooling coverage is inferior in front of the struts due to their upstream blockage effect, which is also evident in the static pressure field.

Fig. 16 presents the circumferentially averaged film cooling effectiveness along the hub and the shroud, averaged in the same manner as Fig. 11. Black lines denote the combined film cooling effectiveness of the FWD and AFT cavities (FWD hub and AFT hub for the hub surface and vice versa). Grey lines denote the single film cooling effectiveness of the FWD cavities, $\eta_{SG,FWD}$. Solid lines denote the hub, and dashed lines denote the shroud.

The contribution of the FWD cavities to the cooling performance in the TCF is below 0.02 for the hub and the shroud and, therefore, negligibly low. As the FWD purge flows pass through the rotor, they are diluted to the extent that they are practically irrelevant for any cooling considerations in the TCF. The circumferentially averaged hub film cooling effectiveness has a maximum of 0.5 at the hub cavity exit and then rapidly drops to $\eta=0.1$ at $s/L_{Hub}=0.25$. The shroud film cooling effectiveness could not be measured until the AFT tip cavity exit due to geometrical restrictions in the placement of the wall taps. However, the wall tap row closest to the cavity exit is located at $s/L_{Hub}=0.016$ and showed a circumferential average of $\eta=0.52$. Likewise, the film cooling effectiveness on the shroud shows a rapid decay, but $\eta=0.1$ is surpassed significantly further downstream at $s/L_{Hub}=0.46$.

The total purge mass flow per circumferential unit span, $M \cdot d$, where M is the blowing ratio and d is the slot width of the cavity, is the decisive parameter when different film cooling configurations shall be compared [9]. Serendipitously, $M \cdot d$ is almost equal for the AFT hub and the AFT tip purge, where $M \cdot d$ is only 10% higher for the AFT hub cavity. Therefore, the film cooling performance of the AFT hub and tip cavities can be coarsely compared in Fig. 16 without nondimensionalization. Considering the cavity geometries in Fig. 4, it is counterintuitive that the perpendicularly injected AFT tip purge flow outperforms the nearly tangentially injected AFT hub purge flow; - especially because the AFT tip purge flow is injected directly upstream of a pronounced convex bend.
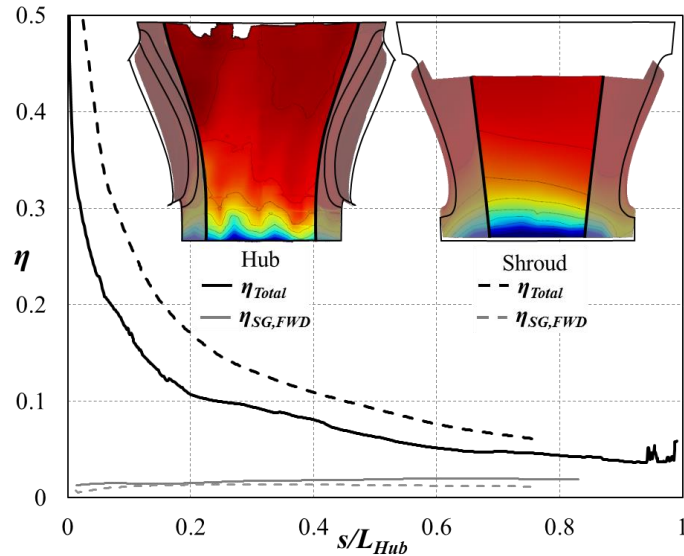

Figure 16: Circumferential average of the film cooling effectiveness along the hub and the shroud surface

However, as explained by Ito et al. [13], cooling flows with lower momentum as the main flow ($I<1$), as is the case in this study, show superior cooling performance on convex and inferior performance on concave walls: To fulfill the equilibrium between the purge flow's momentum divided by the curvature radius of the purge flow path, $\rho V^2/r$, with the global radial pressure gradient in the duct dP/dr, the low momentum purge flow must follow a smaller curvature radius than the surrounding high momentum main flow:

$$\frac{dP}{dr} = \frac{\rho V^2}{r}. \tag{8}$$

This mechanism pushes the low momentum AFT tip purge flow against the convex shroud surface and forces the AFT hub purge flow away from the concave hub surface. The detrimental influence of the HPT vortex pairs on the hub worsens the film cooling performance on the hub additionally.

Another influencing parameter is the streamwise pressure gradient, where the acceleration parameter K in the TCF is approximately -10×10^{-7} after the TCF inlet and then quickly drops to values around -2×10^{-7}. Sivrioglu [36] showed that for slot injection with M=0.28, especially the combination of an adverse pressure gradient with a convex surface leads to increased film cooling effectiveness. Therefore, it is believed that the combination of surface curvature and adverse pressure gradient improves η on the shroud compared to the hub.

Fig. 17 compares the circumferentially averaged η_{IR} of the nominal purge and the CO_2 purge case along the hub surface. This diagram solely serves the purpose of confirming the negligible influence of a different density ratio for low blowing ratios on the film cooling effectiveness. As the η_{IR} curves are virtually collapsing well within the η_{IR} uncertainty, a density ratio influence on η and, as shown in Fig. 11, on h can be ruled out for the given operating parameters. This confirms the consensus stated in the introduction, that the influence of the density ratio is minimal for the low blowing ratios of HPT purge flows [9, 15]. The minor deviations in Fig. 17 can be considered as the repeatability of the IR measurements.

Since it was shown above that the injection of the AFT hub purge air not only led to a cooling benefit but also to a heat transfer intensification on the hub, the heat transfer reduction, Θ, according to Baldauf et al. [37], is shown in Fig. 18. The formula is given in the diagram, where h is the heat transfer coefficient of the nominal purge case, h' is the heat transfer coefficient of the no purge case and $\vartheta = h_{internal}/h'$ is the fraction of the internal heat transfer coefficient (including conduction through the wall) over the external h'. As the flow of the internal coolant of the TCF is less guided than on the flowpath side, the internal heat transfer is assumed to be less than or equal to the external heat transfer; hence Θ is calculated for $\vartheta=0.01$, 0.1 and 1. The data shown in Fig. 18 is for the circumferential hub averaging region used in Fig. 11 and 16 and can be seen as the combination of the hub curves of these figures.

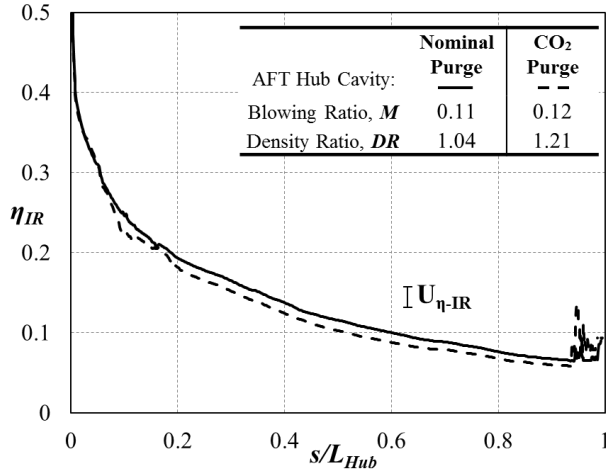| AFT Hub Cavity:	Nominal Purge	CO₂ Purge
Blowing Ratio, M	0.11	0.12
Density Ratio, DR	1.04	1.21

Figure 17: Influence of density ratio: circumferential average of the film cooling effectiveness from IR along the hub surface for nominal and 36% (mass-fraction) CO₂ purge
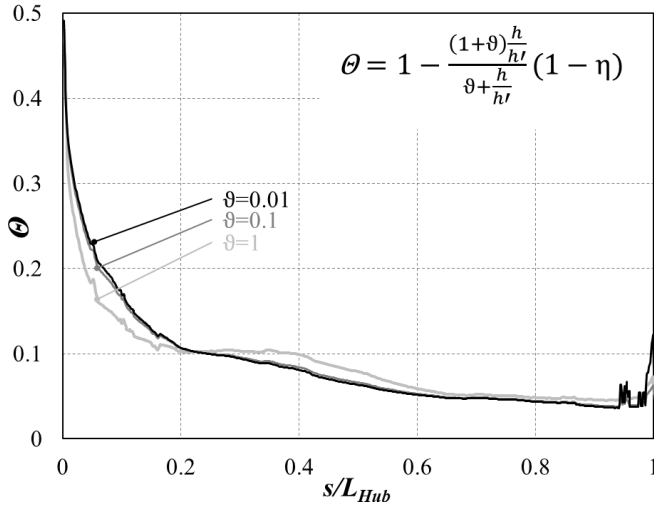

$$\Theta = 1 - \frac{(1+\vartheta)\frac{h}{h\prime}}{\vartheta+\frac{h}{h\prime}}(1-\eta)$$

Figure 18: Circumferential average of the Heat flux reduction along the hub surface

The graph in Fig. 18 shows that the circumferentially averaged Θ is always positive for all ϑ values along the hub. This means that the cooling effect of the AFT hub purge injection always outweighs the heat transfer intensification. The net heat transfer into the TCF hub is reduced by purge injection.

Although not shown here, zones of negative Θ exist at the midspan of both struts, indicating detrimental cooling effects. The midspan of the struts is not reached by any purge flow, but the core flow through the TCF still accelerates due to a mild blockage effect of the injected purge flows. This leads to increased h at the strut midspan without any cooling benefit.

5 CONCLUSIONS

This work presents detailed heat transfer and film cooling measurements in an engine-representative and "aggressive" TCF with a fully purged state-of-the-art single-stage HPT operating

upstream. The heat transfer coefficient on the hub and the non-turning struts was measured using flexible heating foils and infrared thermography. The individual film cooling effectivenesses of all four HPT purge flows emanating from product-representative seal geometries were measured on the hub, the struts and the shroud of the TCF. This cooling effect, sometimes referred to as "phantom cooling", was measured using a hybrid approach, combining infrared thermography and the seed gas concentration technique.

The most remarkable finding is that the distributions of heat transfer coefficient and also film cooling effectiveness form longitudinal streaks on the hub. Furthermore, these high heat transfer and high film cooling streaks are alternately distributed along the circumference. This is a disadvantageous combination, where high heat transfer meets poor cooling. The streaks have the same count as the upstream HPT vanes and are caused by the HPT flow field. The pair of the HPT vane lower passage vortex and the (modulated and split) HPT rotor lower passage vortex is the decisive driver of those streaks. These vortices sustain the high heat transfer streaks throughout the hub and collect the purge flow into discrete bands in between the high heat transfer streaks.

The heat transfer on the struts is heavily governed by the oncoming HPT flow field. The total pressure and velocity fields at the HPT outlet are virtually imprinted on the heat transfer distribution on the struts. The point of highest heat transfer in the TCF is found on the strut and coincides with a local total pressure and velocity maximum in the HPT outlet flow field. The cooling effect of the HPT purge flows on the TCF strut is negligible, as all four purge flows' combined film cooling effectiveness was always below 0.05.

The film cooling effectiveness on the shroud was higher and more evenly distributed than on the hub. The effectiveness maximum on the hub was 0.5, and on the shroud 0.52, both near the cavity exits. The cooling impact of the HPT forward purge flows was inferior, with effectivenesses always below 0.02.

The turbulent flat plate correlations predicted the heat transfer surprisingly well on the hub and the strut surfaces. The circumferentially averaged hub data and the strut midspan data can be predicted with flat plate correlations with a ±10% error, which is given the complex inflow of the HPT and the aerodynamic aggressiveness of the TCF remarkable.

From a design perspective, the first measure would be to adjust the circumferential position of the HPT vanes relative to the TCF struts by half the HPT vane pitch (clocking). This would shift the undisturbed core flow of the HPT vanes away from the strut leading edges and reduce the heat transfer intensity on the struts significantly. Furthermore, this would also reduce the losses generated in the TCF, as found by Sterzinger et al. [29]. The HPT aft purge flows bear a substantial cooling potential on the hub and the shroud close to the cavity exits, which should be considered in future thermal designs. Both measures, clocking the HPT vanes relative to the TCF struts and considering the HPT aft purge flows as cooling films on the TCF hub and shroud during the design phase, allow for a further increase in turbine inlet temperature from the perspective of the TCF.

13

ACKNOWLEDGEMENTS

NOMENCLATURE

ACR	advective capacity ratio $(=c_{p,P}\,\rho_P\,V_P\,/c_{p,M}\,\rho_M\,V_M)$
c	strut chord length (m)
c_P	specific isobaric heat capacity (J/kgK)
$conc.$	seed gas concentration (CO_2 or N_2O)
DR	density ratio (= ρ_P/ρ_M)
d	cavity exit slot width (m)
H	channel height (m)
h	heat transfer coefficient (W/m^2K), coordinate along channel height, H (m)
I	momentum flux ratio (= $\rho_P\,V_P^2/\rho_M\,V_M^2$)
k	thermal conductivity (W/mK)
K	acceleration parameter ($=v/V_\infty^2 \times dV_\infty/ds$)
L	axial length of TCF (m)
L_{Hub}	unwound hub length (m)
M	blowing ratio (= $\rho_P\,V_P/\rho_M\,V_M$)
Ma	Mach number
$\dot{m}$	mass flow rate (kg/s)
Nu_s	local Nusselt number (= $h_s s/k$)
n	rotational speed (rpm)
P	pressure (mbar)
Pr	Prandtl number
$\dot{q}$	heat flux (W/m^2)
r	radius (m)
Re_c	Reynolds number based on strut chord length (= $V_\infty c/v$)
Re_s	Reynolds number based on local coordinate s (= $V_\infty s/v$)
s	coordinate along strut chord or hub (m)
T	temperature (K)
U_F	uncertainty in parameter F
V	absolute velocity (m/s)
α	surface angle ($degrees$)
Δr	radius difference (m)
ε	emissivity
η	adiabatic film cooling effectiveness
Θ	heat transfer reduction, Baldauf et al. [37]
v	kinematic viscosity (m^2/s)
π	total pressure ratio
ρ	density (kg/m^3)
τ	transmissivity
ω_{sw}	streamwise vorticity ($1/s$)

Subscripts

ad	(quasi) adiabatic	W	window
in	inlet	x,t,r	cyl. coordinates
IR	from infrared	0	total
M	mainstream	∞	freestream
out	outlet	S	surface or static
P	purge	SG	from seed gas

Superscripts

$'$	no purge case

REFERENCES

[1] European Environment Agency, European Union Aviation Safety Agency and EUROCONTROL, 2019, "European Aviation Environmental Report 2019", doi: 10.2822/309946

[2] European Commission, Directorate-General for Mobility and Transport, Directorate-General for Research and Innovation, 2011, "Flightpath 2050: Europe's vision for aviation: maintaining global leadership and serving society's needs", Publications Office, doi: 10.2777/50266

[3] Grewe, V., Gangoli Rao, A., Grönstedt, T. et al., 2021, "Evaluating the climate impact of aviation emission scenarios towards the Paris agreement including COVID-19 effects", Nat Commun 12, 3841 (2021), doi: 10.1038/s41467-021-24091-y

[4] GE Aerospace, "GE9X Commercial Aircraft Engine", accessed November 21, 2019, https://www.geaviation.com/commercial/engines/ge9x-commercial-aircraft-engine

[5] MTU Aero Engines AG, "Mittendrin, das Turbinenzwischengehäuse für Großtriebwerke", MTU AEROREPORT, accessed Sep. 15, 2022, https://aeroreport.de/de/innovation/mittendrin-das-turbinenzwischengehaeuse-fuer-grosstriebwerke

[6] Graziani, R. A., Blair, M. F., Taylor, J. R., and Mayle, R. E., 1980, "An Experimental Study of Endwall and Airfoil Surface Heat Transfer in a Large Scale Turbine Blade Cascade," ASME Journal of Engineering for Power, Vol.102, pp. 257-267.

[7] Hylton, L. D., Mihelc, M. B., Turner, E. R., Nealey, D. A., and York, A., "Analytical and Experimental Evaluation of the Heat Transfer Distribution Over the Surfaces of Turbine Vanes," NASA CR 168015, Final Report for Contract No. NAS3-22761.

[8] Hartnett, J.P., Birkebak, R.C., Eckert, E.R.G., 1961, "Velocity Distributions, Temperature Distributions, Effectiveness and Heat Transfer for Air Injected Through a Tangential Slot Into a Turbulent Boundary Layer", J. Heat Transfer, Aug 1961, 83(3): 293-305

[9] Bogard, D.G., Thole, K.A., 2006, "Gas Turbine Film Cooling", AIAA J. Propulsion and Power Vol. 22, pp 249-270, doi: 10.2514/1.18034

[10] Thole, K. A., Knost, D. G., 2005, "Heat Transfer and Film-Cooling for the Endwall of a First Stage Turbine Vane", Int. J. of Heat and Mass Transfer, 48(25–26): 5255-5269.

[11] Suryanarayanan, A., Mhetras, S. P., Schobeiri, M. T., and Han, J. C., 2008, "Film-Cooling Effectiveness on a Rotating Blade Platform", ASME. J. Turbomach. January, 131(1): 011014.

[12] Zerobin, S., Aldrian, C., Peters, A., Heitmeir, F., and Göttlich, E., 2017, "Impact of Individual High-Pressure Turbine Rotor Purge Flows on Turbine Center Frame Aerodynamics", ASME Paper GT2017-63616.

14

[13] Ito, S., Goldstein, R. J., and Eckert, E. R. G., 1978, "Film Cooling of a Gas Turbine Blade.", ASME. J. Eng. Power. July 1978, 100(3), 476–481, doi: 10.1115/1.3446382

[14] Hummel, T., Kneer, J., Schulz, A. und Bauer, H.-J., 2015, "Experimentelle Untersuchung des Wärmeübergangs und der Filmkühleffektivität einer dreidimensionalen konturierten Turbinen-seitenwand", Deutscher Luft und Raumfahrtkongress 2015, urn:nbn:de:101:1-201601293626

[15] Sinha, A. K., Bogard, D. G., Crawford, M. E., 1991, "Film-Cooling Effectiveness Downstream of a Single Row of Holes with Variable Density Ratio", ASME J. Turbomach. July, pp. 442-449.

[16] Fischer, J. P., McNamara, L. J., Rutledge, J. L., and Polanka, M. D.,2020, "Scaling Flat-Plate, Low-Temperature Adiabatic Effectiveness Results Using the Advective Capacity Ratio.", ASME. J. Turbomach. August 2020, 142(8):081010. doi: 10.1115/1.4046544

[17] Göttlich, E., 2011, "Research on the Aerodynamics of Intermediate Turbine Diffusers", Progress in Aerospace Sciences, 47(4): 249-279.

[18] Zerobin, S, Peters, A, Bauinger, S, Ramesh, A, Steiner, M, Heitmeir, F, & Göttlich, E, 2017, "The Behavior of Turbine Center Frames Under the Presence of Purge Flows.", Proceedings of the ASME Turbo Expo 2017 doi: 10.1115/GT2017-63606

[19] Patinios, M, Merli, F, Hafizovic, A, & Göttlich, E, "The Interaction of Purge Flows With Secondary Flow Features in Turbine Center Frames.", Proc. ASME Turbo Expo 2021, V02CT35A002, doi: 10.1115/GT2021-58586

[20] Arroyo Osso, C., Johansson, T. G., and Wallin, F., 2010, "Heat Transfer Investigation of an Aggressive Intermediate Turbine Duct: Part 1—Experimental Investigation", ASME Paper GT2010-23653.

[21] Jagerhofer, P. R., Patinios, M., Erlacher, G., Glasenapp, T., Göttlich, E., and Farisco, F., 2021, "A Sector-Cascade Test Rig for Measurements of Heat Transfer in Turbine Center Frames.", ASME. J. Turbomach. July 2021, 143(7): 071015, doi: 10.1115/1.4050432

[22] Steiner, M., 2018, "Einfluss der Zuströmung auf den Turbinenübergangkanal", PhD thesis, Graz University of Technology.

[23] Jagerhofer, P. R., Patinios, M., Glasenapp, T., Göttlich, E., and Farisco, F., 2022, "The Influence of Purge Flow Parameters on Heat Transfer and Film Cooling in Turbine Center Frames.", ASME. J. Turbomach. July 2022, 144(7): 071001, doi: 10.1115/1.4053235

[24] Jagerhofer, P. R., Woisetschläger, J., Erlacher, G., and Göttlich, E., 2021, "Heat transfer and film cooling measurements on aerodynamic geometries relevant for turbomachinery. ", SN Appl. Sci. 3, 889 (2021), doi: 10.1007/s42452-021-04845-5

[25] Erhard, G., and Gehrer, A., 2000, "Design and Construction of a Transonic Test-Turbine Facility" Proceedings of the ASME Turbo Expo 2000, Munich, Germany, May 8–11.

[26] Neumayer, F., Kulhanek, G., Pirker, H., Jericha, H., Seyr, A., and Sanz, W., 2000, "Operational Behavior of a Complex Transonic Test Turbine Facility", Proceedings of the ASME Turbo Expo 2001, New Orleans, LA, June 4–7.

[27] Steiner, M., Zerobin, S., Bauinger, S., Heitmeir, F., and Göttlich, E., 2017, "Development and Commissioning of a Purge Flow System in a Two Spool Test Facility", 12th European Conference on Turbomachinery Fluid dynamics & Thermodynamics, Stockholm, Sweden, Apr. 3–7.

[28] Faustmann, C., and Göttlich, E., 2014, "Aerodynamics and Acoustics of Turning Mid Turbine Frames in a Two-Shaft Test Turbine". ASME Paper No. GT2014-25568. Düsseldorf, Germany, June 16-20, 2014.

[29] Sterzinger, P. Z., Merli, F., Peters, A., Behre, S., Heitmeir, F., and Göttlich, E., 2021, "Impact of Turbine-Strut Clocking on the Performance of a Turbine Center Frame." ASME. J. Turbomach. May 2021, 143(5): 051011. doi: 10.1115/1.4050145

[30] McNamara, L. J., 2019, "Scaling Film Cooling Adiabatic Effectiveness with Mass Transfer and Thermal Experimental Techniques", Theses and Dissertations, 2227, https://scholar.afit.edu/etd/2227

[31] Sellers, J. P., Jr., 1963, "Gaseous Film Cooling With Multiple Injection Stations," AIAA J., 1(9), pp. 2154–2156.

[32] "Evaluation of measurement data — Guide to the Expression of Uncertainty in Measurement", JCGM 100:2008, in GUM series of JCGM. Accessed February 2020.

[33] Gregory-Smith, D. G., Graves, C. P., and Walsh, J. A., 1988, "Growth of Secondary Losses and Vorticity in an Axial Turbine Cascade." ASME. J. Turbomach. January 1988; 110(1): 1–8, doi: 10.1115/1.3262163

[34] Çengel, Y. A., & Ghajar, A. J., 2011, "Heat and Mass Transfer: Fundamentals & Applications", New York, McGraw-Hill.

[35] Sibson, R., 1981 "A brief description of natural neighbor interpolation (Chapter 2)" Barnett V (ed) Interpreting multivariate data, John Wiley, Chichester, pp 21–36

[36] Sivrioglu, M., 1991 "An analysis of the effects of pressure gradient and streamline curvature on film cooling effectiveness" Wärme- und Stoffübertragung, vol. 26, no. 2, pp. 103–107, doi: 10.1007/BF01590243

[37] Baldauf, S., Scheurlen, M., Schulz, A., Wittig, S., 2002, "Heat Flux Reduction From Film Cooling and Correlation of Heat Transfer Coefficients From Thermographic Measurements at Enginelike Conditions" ASME. J. Turbomach. October 2002; 124(4): 699–709. doi: 10.1115/1.1505848